Nanoscale

ROYAL SOCIETY OF CHEMISTRY

PAPER

View Article Online
View Journal | View Issue

Cite this: *Nanoscale*, 2025, **17**, 14248

From Co to Co@Co_2P and CoP nanorods: synthesis and performances in selective hydrogenation of phenylacetylene†

Brandon Azeredo,[a] Jason Nguyen-Cong,[a] Mathieu Vidal,[b] Seema Shafiq,[a,b] Thi Thiet Vu,[a] Beatrice Muzzi,[a] Audrey Marty,[a] Yuanyuan Min,[a] Fabio Ferrari,[a] Fabien Delpech,[a] Céline Nayral,[a] Pier-Francesco Fazzini,[a,c] Thomas Blon,[a] Philippe Serp,*[b,d] Guillaume Viau*[a] and Katerina Soulantica*[a]

Received 11th February 2025,
Accepted 28th April 2025

DOI: 10.1039/d5nr00618j

rsc.li/nanoscale

Transition metal phosphides are emerging catalysts for reactions traditionally catalyzed by noble metals. Cobalt phosphide nanostructures are currently intensively studied as electrocatalysts, but their catalytic properties in thermocatalytic reactions are much less explored. Here we report the topochemical reaction of ferromagnetic metallic cobalt nanorods with tris(trimethylsilyl) phosphine (PTMS) at 165 °C, which leads to the conservation of the nanorod shape while transforming them to Co@Co_2P core@shell nanorods. The Co_2P shell thickness can be controlled through the PTMS/Co ratio. Modulation of the core–shell structure allows tuning the magnetic properties of the resulting nano-objects. Increasing both the temperature and PTMS/Co ratio results in the complete transformation of Co into well-crystallized CoP nanorods. The catalytic performances Co@Co_2P and CoP nanorods in the selective hydrogenation of phenylacetylene have been evaluated. It is shown that increasing the P/Co ratio in the nanorods allows increasing both the activity and the selectivity to styrene. Comparison with cobalt phosphide nanoparticles reported in the literature for the selective hydrogenation of phenylacetylene shows the superior performance of the Co@Co_2P and CoP nanorods prepared in this work.

1. Introduction

Phosphides of transition metals (TMPs) are active and stable heterogeneous catalysts for hydroprocessing processes such as hydrodesulfurization, hydrodenitrogenation and hydrodeoxygenation reactions.[1–3] As the incorporation of phosphorus into transition metals induces electronic, geometric and synergetic effects, which are currently actively explored, TMPs are intensely studied as cost-efficient, Earth abundant electrocatalysts[4–6] or alternative anode materials for lithium-ion batteries,[7,8] and also in photo- and thermocatalysis.[9–11]

As the transition from bulk to nanoscale offers the possibility to exploit new properties or performance improvements resulting from the nanoscale dimensions,[12,13] different methods have been developed to prepare nanostructured TMPs with controllable size and morphology.[9,14,15] In this context, solution phase synthesis methods are well-adapted for achieving a high degree of control over size, size monodispersity, morphology, crystal structure and composition of inorganic nanoparticles (NPs).[16] Over the last two decades, Co_xP_y NPs of different sizes, shapes and crystal structures have been prepared by different methods.[9,17–23] The most widely employed strategies for the synthesis of highly monodisperse shape controlled Co_xP_y NPs consist in (i) thermal decomposition in high boiling point solvents of molecular cobalt precursors in the presence of surfactants and a P source,[24–26] or (ii) the use of preformed Co NPs as templates that are subsequently subjected to a reaction with a P source.[27,28,34] In the latter case, hollow nanostructures usually result from the Kirkendall effect.[27,28] Among the organophosphorus compounds which are largely employed for the synthesis of well-defined Co_xP_y nanostructures, tri-*n*-octylphosphine (TOP) is the most common one.[22,25,26] Other phosphines such as triphenylphosphine,[29] aminophosphines[30] or $P(SiMe_3)_3$[31] have

[a]*Université de Toulouse, Laboratoire de Physique et Chimie des Nano-Objets (LPCNO) UMR 5215, INSA, UPS, CNRS, 135 avenue de Rangueil, Toulouse F-31077, France. E-mail: ksoulant@insa-toulouse.fr, gviau@insa-toulouse.fr*
[b]*Université de Toulouse, Laboratoire de Chimie de Coordination (LCC) UPR 824, Toulouse INP, CNRS LCC, composante ENSIACET, 4 allée Emile Monso, Toulouse F-31030, France. E-mail: philippe.serp@ensiacet.fr*
[c]*Université de Toulouse, CEMES-CNRS, CNRS, 29 rue Jeanne Marvig, 31055 Toulouse, France*
[d]*Institut Universitaire de France (IUF), France*
† Electronic supplementary information (ESI) available. See DOI: https://doi.org/10.1039/d5nr00618j

also been used. Tri-*n*-octyl phosphine oxide (TOPO)[21,22,32,33] and triphenylphosphite[34–36] can also act as organophosphorus sources. In most of the cases, reaction temperatures of about 300 °C are employed. Depending on the reaction conditions, the degree of phosphidization can be controlled toward Co_2P or CoP nanostructures.[18,22,28,30] Several syntheses afford Co_2P nanorods (NRs),[25,29,33–38] and less CoP NRs.[39–41] However, no core shell Co@Co_xP_y has been reported up to now.

Among TMPs, cobalt phosphide (Co_xP_y) nanostructures have received increasing attention as electrocatalysts for the hydrogen evolution reaction (HER),[27–29,32,42] the oxygen reduction reaction (ORR) over a wide pH range,[33] and dual-function ORR and oxygen evolution reaction (OER) catalysts for zinc–air batteries.[43] On the other hand, their performances in thermocatalytic reactions such as reductive molecular transformations are much less explored.[24,34,35,44,45] The removal of phenylacetylene (PhA), an impurity present in the styrene (ST) feed monomer, by selective semi-hydrogenation is an important process for the polymer industry. Indeed, PhA constitutes a poison that deactivates polymerization catalysts in polystyrene production units.[46] The major challenges in this selective hydrogenation reaction are avoiding the complete hydrogenation to ethylbenzene (EB) and maximizing the selectivity towards ST. Although Pd-based catalysts, in spite of their high cost, are regarded as the top-performing catalysts for this reaction,[47] research is being carried out to find substitutes based on non-noble metals such as nickel[48,49] or cobalt.[50,51] In addition to the cost of the catalysts, these research studies are justified by the fact that, for many unmodified Pd-based catalysts, ST is easily hydrogenated to EB during the pre-desorption process, resulting in low ST selectivity at high PhA conversions.[52,53] On the other hand, metallic (zero-valent) Co and Ni catalysts present serious air instability issues (pyrophoricity), which results in difficult catalyst handling, and chemical process safety issues.[54] The use of their phosphides, which are stable in air, eliminates the need for strict anaerobic conditions or pre-reduction. Although non-noble metal phosphide catalysts have shown interesting performances for hydrogenation reactions,[10,55,56] few results have been reported so far for PhA selective hydrogenation. The published studies mainly deal with nickel phosphide catalysts,[54,57–61] and to a less extent with cobalt phosphide.[62] In the case of nickel phosphide, it was shown that the electron transfer that occurs from Ni to P (resulting in a positively charged Ni) reduces the desorption energy of the alkene and thus improves the reaction selectivity.[60] Indeed, the electron-withdrawing effect of phosphorus in metal phosphides is one of the most important electronic effects (ligand effects) that modulates the electronic environment surrounding the metal sites and distinguishes metal phosphides from other catalysts.[10]

We report here the synthesis of Co@Co_2P and CoP nanorods by a topochemical reaction between tris(trimethylsilyl) phosphine (PTMS) and Co nanorods with a hexagonal close packed (hcp) structure, prepared by an organometallic route. This method allows tuning the thickness of the Co_2P shell on Co up to the complete transformation of Co into Co_2P and CoP. We also present the performances of the Co@Co_2P core@shell and CoP nanorods in the selective hydrogenation of PhA.

2. Experimental section

All syntheses were carried out under an inert atmosphere, either using standard Schlenk techniques or in a glovebox. Oleylamine (Acros Organics 80–90%) and toluene (Fisher Scientific, >99%) were purged by Ar bubbling before introducing them into a glovebox. The tris(trimethylsilyl) phosphine (PTMS) was purchased from STREM (98%). They were introduced in the glove box and used without further purification. *Note*: tris(trimethylsilyl) phosphine (PTMS) catches fire spontaneously if exposed to air and causes eye, skin and respiratory irritation. It has to be handled under an inert atmosphere under a fume-hood, wearing protective gloves, protective clothing and eye protection.

2.1. Bare Co nanorod synthesis

Bare Co nanorods (Co-NRs) were synthesized by a slightly modified published method.[63] In a typical reaction, in a Fischer–Porter reactor in the interior of a glovebox, 1.642 g (6.8 mmol) of hexadecylamine (HDA) was dissolved in 60 mL of a toluene/anisole 5 : 3 mixture. Once HDA was completely dissolved, 0.801 g (4 mmol) of lauric acid (LA) was dissolved in 8 mL of the same toluene/anisole mixture and then added to the HDA solution, forming a white gel-like suspension. A solution of 1.807 g (4 mmol) of the Co precursor [Co{N($SiMe_3$)$_2$}$_2$(thf)] in 12 mL of the toluene/anisole mixture was added to the HDA-LA mixture. The reactor was removed from the glovebox and transferred to a vacuum line where it was evacuated and then pressurized with H_2 to 3 bar. The mixture was heated at 110 °C under stirring for 48 hours. At the end of the reaction, the H_2 was removed, the reactor was transferred in the glovebox, and the nanorods were separated from the Co nanospheres formed during the synthesis, through several washing steps with toluene. Finally, the Co-NRs were dispersed in 20 mL of toluene and stored in a freezer inside the glovebox. Known volumes of the resulting dispersion were used for the subsequent reactions with PTMS. The Co content per mL of the Co-NR suspensions was calculated from magnetic measurements on a dried sample of known volume. The organometallic method gives rise to Co-NRs with diameters and lengths that can slightly vary from one batch to the other. The dimensions of the different batches of Co-NRs that were used as starting materials for each phosphidized product are shown in Table S1.†

2.2. Reaction of bare Co-NRs with PTMS

In a typical reaction, in a three-neck flask equipped with a refrigerant, thermocouple and mechanical stirrer, the bare Co-NRs (0.68 mmol Co) were dispersed in 12 mL of mesitylene. A solution of HDA 82.1 mg (0.34 mmol) in 3.3 mL of mesitylene was added to this mixture and the mixture was heated to

160 °C. Different PTMS amounts in 1.7 mL of mesitylene were injected into the Co-NR suspension when the temperature reached 160 °C. The temperature was increased to 165 °C and the mixture was then let to react at this temperature either for 90 min or for 3 h. The mixture was then allowed to cool down before transferring it to a glovebox where it was let to decant. The supernatant was removed and the precipitate was washed two times with 5 mL of toluene. Complete evaporation of the solvent gave rise to powders that were used for the characterization and for catalysis.

In some cases, and in order to reach higher reaction temperatures, mesitylene was replaced by oleylamine. In these cases, PTMS in oleylamine was injected at 150 °C, and the mixture was kept at this temperature for 30 min, followed by an increase in the temperature to 250 °C, and continuation of the reaction at 250 °C for three hours. The rest of the procedure was identical to the procedure followed with mesitylene as a solvent.

No other nano-objects are formed during phosphidization and the reaction is quantitative with respect to the Co introduced in the reaction.

The samples are named as **Co-P$_{x/y}$** where x corresponds to the P/Co ratio introduced and y to the reaction temperature (165 or 250 °C).

2.3. Characterization

The magnetic properties of the starting Co-NRs and the nanostructures obtained after the reactions were studied by vibrating sample magnetometry (VSM) using a Quantum Design PPMS 9T Evercool II magnetometer system. To avoid any oxidation, the samples were prepared in a glovebox, and transferred to a cryostat VSM in a Schlenk vessel. Standard VSM capsules were filled with a known amount (a few mg) of vacuum-dried sample, mixed with tetracosane as a solid matrix, and sealed. The VSM capsules containing the samples were rapidly introduced into the VSM in order to avoid air-exposure of the sample. A field-dependent (±6 T) magnetization cycle at 300 K was recorded in the first step. The saturation magnetization (M_s) of the Co nanorods was compared to the M_s value of Co (160 A m^2 kg^{-1}) at room temperature (RT), which allows the determination of the Co(0) wt% content in the sample. A second field-dependent magnetization cycle was recorded after cooling the sample down to 5 K (FC) while applying +6 T (FC) and allows the detection of Co-oxidation. The presence of CoO on the surface of Co provokes a shift of the 5 K magnetization loop because of an exchange bias between the antiferromagnetic CoO and the ferromagnetic Co.

X-Ray diffraction (XRD) experiments have been performed on a Malvern Panalytical Empyrean diffractometer, equipped with a Co anticathode X-ray source (Co Kα = 1.790 Å), a Bragg–Brentano HD mirror and a PIXCel1D detector. To avoid any oxidation, the samples were encapsulated between two thin layers of Kapton® film. For the well-crystallized **Co-P$_{3/250}$** NRs, XRD analysis was carried out using the MAUD software[64] based on the Rietveld method combined with Fourier analysis.

Routine transmission electron microscopy (TEM) analyses were performed in the Microcharacterization Center Raymond Castaing, on a JEOL 1011 microscope operating at 100 kV and a JEOL 1400 microscope operating at 120 kV equipped with a camera ORIUS 1000 GATAN. Both microscopes are equipped with a tungsten filament as the emission source. High-resolution TEM (HRTEM) was performed on two microscopes, an ARM200F Cold FEG spherical aberration corrected (Cs) at 200 kV (1.9 Å resolution) and a JEOL 2100F using a Schottky field emission gun at 200 kV (2.3 Å resolution). The images were collected using a GATAN ULTRASCAN 2k × 2k Model 994 (ARM) camera and a CMOS GATAN RIO16IS 4k × 4k (2100F) camera. Scanning TEM (STEM) images (0.78 Å resolution) and energy dispersive X-Ray spectroscopy (EDX) analyses were carried out on a JEOL-ARM200F Cold FEG mounted with a EDX SDD CENTURIO-X (129 eV resolution). The samples were prepared by dropping a diluted solution on a carbon-coated copper grid. The grids were systematically evaporated using a pump (P = 5.10^{-4} mbar) to remove excess volatile residues.

The X-ray photoelectron spectroscopy (XPS) analyses were performed on samples prepared by depositing a few drops of the suspended solids on a Si wafer followed by solvent evaporation. The spectra were recorded using a K-alpha plus system (Thermo Fisher Scientific, East-Grinstead, UK) fitted with a micro-focused and monochromatic Al Kα X-ray source (1486.6 eV, spot size of 400 μm). The spectrometer pass energy was set to 150 and 40 eV for the survey and the narrow high-resolution regions, respectively.

ICP analyses were performed by Microanalytical Laboratory Kolbe.

2.4. Catalysis

Supported catalyst preparation. A few-layer graphene (FLG) support (Avanzare avanPLAT-7) was used after oxidation by boiling in nitric acid for 3 h.[65] The TiO_2 support ($TiO_{2\text{-}P25}$, Evonik) was used as received. An impregnation method was used to prepare the cobalt catalysts supported on oxidized FLG and titania in a glovebox. The desired mass of NRs (Co content measured by ICP), was added to THF (30 mL) to introduce 5% w/w of Co with respect to the support, and then 1 g of oxidized FLG or TiO_2 was added. The solution was then stirred for 2 h and dried overnight under vacuum, and the whole process was conducted under an inert atmosphere. The catalysts were used as prepared.

Test to assess H-spillover. To check for H-spillover, WO_3 was used to diagnose the activation of H_2 in the catalysts, because the spilt-over H species migrates and readily reacts with the yellow WO_3 to form dark blue H_xWO_3. The WO_3 powder (1 g) was mixed with the catalyst (10 mg) and treated under the reaction conditions employed in catalysis in the absence of PhA and in the presence or absence of water.

Catalytic hydrogenation of phenylacetylene in a batch reactor. Hydrogenation reactions were performed in a Top Industrie high-pressure and temperature stainless-steel autoclave equipped with a controlling system for temperature and

pressure. In a typical experiment, a mixture containing the catalyst, 30 mL of a phenylacetylene solution in methanol (PhA/Co = 500, 2 mmol of PhA,) and decane (75 mg) as an internal standard, were transferred into the autoclave in the interior of a glove box after brief sonication. The autoclave was then removed from the glovebox and connected to a vacuum line, purged by three vacuum/H_2 cycles, heated at 90 °C or 100 °C and pressurized with H_2 to 5 bar. The stirring rate was fixed at 700 rpm to avoid mass transfer limitations. For the tests performed at 90 °C, the reaction was followed for 24 hours, taking a sample every 2 hours. For the tests performed at 100 °C, the reaction was followed for 6 hours taking a sample every hour. Liquid phase analysis was made offline periodically, thanks to GC-FID equipment. To evaluate the effect of water on catalysis, some tests were performed adding 1 mL of water to the autoclave, after connection to the vacuum line.

The catalyst performance was evaluated by measuring the site time yield (STY, in $mol_{PhA}\ mol_{Co}^{-1}\ h^{-1}$) (eqn (1)) and styrene selectivity at isoconversion ($S_{ST\text{-}x\%conversion}$ in %) (eqn (2)).

$$STY = \frac{(mol_{PhA})}{(mol_{Co})xt} \quad (1)$$

where mol_{PhA} is the number of moles of PhA converted at a given time t; mol_{Co} is the number of moles of Co introduced (from ICP-OES analysis); and t is the reaction time.

$$S_{ST-x\%\,conversion} = \frac{mol_{ST}}{mol_{PhA\,converted}} \quad (2)$$

where mol_{ST} is the number of moles of ST formed at a given conversion of x%; and $mol_{PhA\ converted}$ is the number of moles of PhA converted at a given conversion of x%.

Recycling experiments. Recyclability tests were performed to assess the stability and reusability of two cobalt-based catalysts – **Co-P$_{3/250}$/TiO$_2$** and **Co-P$_{3/250}$/FLG**. All experiments were conducted in a batch reactor. In the interior of a glove-box, the catalyst powders were charged in an autoclave reactor vessel. For the first catalytic cycle, the required amounts of catalyst, PhA, and decane (used as an internal standard) were weighed and loaded into the reactor, maintaining a high PhA-to-cobalt ratio so as to reach a relatively low conversion (typically < 15%) in 6 hours. The sealed reactor was then removed from the glovebox, charged with 30 mL of methanol, and subjected to hydrogenation at 100 °C under 5 bar H_2 pressure for 6 hours in the batch reactor. Upon completion of each reaction, the mixture was analysed by gas chromatography with flame ionization detection (GC-FID) to determine the conversion and selectivity. The catalyst was separated from the reaction mixture by vacuum filtration using a Schlenk line, washed with methanol, dried, weighed and then stored overnight under a nitrogen atmosphere. No additional treatments were applied before reuse; the catalyst was employed directly in the subsequent cycle maintaining a constant PhA-to-cobalt ratio in all recycling runs.

3. Results and discussion

The reaction of Co-NRs was explored with tris(trimethylsilyl) phosphine (PTMS), a reactive precursor that has been used efficiently for the synthesis of metal phosphides under relatively mild reaction conditions.[31,66,67] Fig. S1a† shows a characteristic TEM image and the XRD pattern of the raw Co-NRs used as the starting material. Their mean diameter d_m and mean length L_m were determined from TEM image analysis. The dimensions of the different batches of Co-NRs that were used are presented in Table S1.† The Co-NRs crystallize in the hcp structure of bulk Co. Their XRD pattern (Fig. S1b†) shows a strong anisotropy, the two broad peaks at 49° and 56° correspond to the $(10\bar{1}0)$ and $(10\bar{1}1)$ reflections of hcp Co, while the narrow peak at 52° corresponds to the (0002) reflection, which shows a higher coherence length along the c axis indicating that the c-axis of the hcp structure lies along the nanorod long axis.

The Co-NRs were first treated with PTMS at two Co : P ratios 1 : 0.2 (**Co-P$_{0.2/165}$**) and 1 : 0.7 (**Co-P$_{0.7/165}$**). PTMS was injected in the Co-NR dispersion in mesitylene at 160 °C, the temperature was increased to 165 °C and kept at 165 °C for 90 min. TEM observations showed that the resulting nano-objects retained their shape after the reaction for both ratios (Fig. 1a and b). While the **Co-P$_{0.2/165}$** NRs (Fig. 1a) exhibited the same contrast aspect as the starting Co-NRs; darker areas at the center of the **Co-P$_{0.7/165}$** NRs indicate the formation of a core@shell structure (Fig. 1b).

The XRD data for both ratios are presented in Fig. 1c. For the **Co-P$_{0.2/165}$** NRs, the diffractogram mainly indicates the presence of hcp Co but some reflections of Co_2P can be distinguished from the background, while these latter are more pronounced for the **Co-P$_{0.7/165}$** NRs. Only hcp Co could be observed in HRTEM for the **Co-P$_{0.2/165}$** NRs (Fig. S2a and b†), but scanning transmission electron microscopy-high angle annular dark field (STEM-HAADF) analysis (Fig. S2c†) clearly shows the presence of a denser core, which corresponds to hcp Co and a less dense shell attributed to poorly crystallized Co_2P, in agreement with the XRD results. STEM-HAADF of **Co-P$_{0.7/165}$** NRs shows a very similar configuration (Fig. S2f†). EDX mapping of **Co-P$_{0.2/165}$** (Fig. S2d and e†) and **Co-P$_{0.7/165}$** (Fig. S2g and h†) lying flat on the TEM grid does not allow a clear distinction between the core and the shell. Indeed, the difference in the relative concentration of Co (higher in the core area but present also in the shell) is not high enough to clearly evidence the differences between the core and the shell. However, for the **Co-P$_{0.7/165}$** NRs, both the STEM-HAADF image (Fig. 2a) and the bright field image (Fig. 2b) on an NR array with the long NR axes oriented parallel to the electron beam clearly evidence the core–shell structure. EDX line analysis, confirmed the core–shell structure, with a Co core of roughly 2 nm and a 1.5 nm thick Co_2P shell (Fig. 2a). As expected for a Co@Co_2P configuration, the Co signal is maximized at the core area (brighter area highlighted by the white dotted line in Fig. 2a), and is reduced on the shell, while the opposite is observed for the P signal. In this configuration, the difference

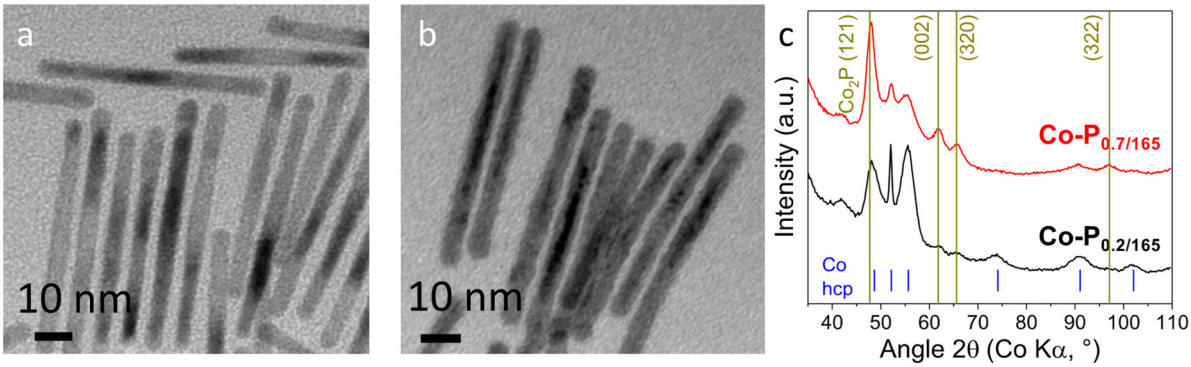

Fig. 1 TEM images of (a) **Co-P$_{0.2/165}$** NRs and (b) **Co-P$_{0.7/165}$** after 90 min reaction. (c) XRD diffractograms of the **Co-P$_{0.2/165}$** and **Co-P$_{0.7/165}$** NRs. Blue and olive-green lines correspond to the expected reflections of hcp-Co (COD file 9008492, *P*63/*mmc*, *a* = 2.507 Å, *c* = 4.068 Å) and orthorhombic Co_2P (COD file 9009202, *Pnam*, *a* = 5.646 Å, *b* = 6.608 Å, *c* = 3.513 Å), respectively.

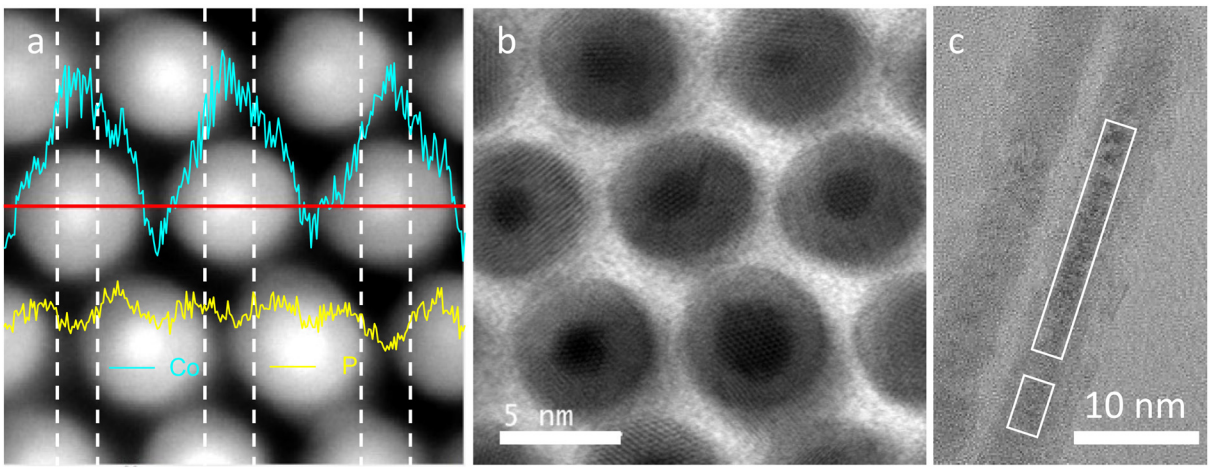

Fig. 2 **Co-P$_{0.7/165}$** NRs. (a) Overlay of an EDX line analysis (Co: cyan; P: yellow) and a dark field HAADF image of an assembly of nanorods oriented parallel to the electron beam (top view). (b) Top view bright field image of the same nanorods showing the core@shell Co@Co_2P configuration. (c) HRTEM side view image of two NRs. The white rectangles represent domains where the Co hcp structure persists.

in Co and P concentrations between the core and the shell is revealed. As the beam crosses the whole length of the NRs, the Co core signal is much more intense, as compared to the minor contribution to the signal of P present on the shell of the extremities. These nanorods are composed of a crystalline hcp Co core and a partially crystalline Co_2P shell. However, the Co core is sometimes fragmented as discerned in Fig. 1b, and as explicitly illustrated by HRTEM in Fig. 2c.

The magnetic properties of the **Co-P$_{0.2/165}$** and **Co-P$_{0.7/165}$** NRs were compared to the initial Co-NRs (Fig. 3). As expected from the transformation of the ferromagnetic hcp Co into paramagnetic Co_2P,[68] the saturation magnetization M_s of the sample decreases as the amount of injected PTMS increases, that is, from 123 A m^2 kg^{-1} for the starting Co-NRs to 59 and 24 A m^2 kg^{-1} for **Co-P$_{0.2/165}$** and **Co-P$_{0.7/165}$**, respectively (Fig. 3a and Table S2† entries 2 and 3 respectively). Considering that the magnetization of Co_2P is negligible,[68] it is obvious from these magnetic measurements that Co(0) is still present in the core, which indicates that the transformation reaction is not complete, in agreement with the core–shell structure observed by TEM. From the M_s values, we can evaluate the Co(0) amount that remains intact in each sample and from ICP analyses that give the total Co amount, we can deduce the percentage of Co transformed in each sample. Interestingly, while for **Co-P$_{0.2/165}$** (Table S2,† entry 2) the experimentally calculated composition is very close to the theoretical composition, for the **Co-P$_{0.7/165}$** NRs, the incorporation of P in the Co-NRs is incomplete (Table S2† entry 3). Indeed, the use of a slight excess of PTMS (Co/P = 1/0.7) as compared to the stoichiometric Co/P ratio of 1/0.5, is not sufficient to completely convert Co into Co_2P under the conditions employed.

The coercive fields follow the same trend as the magnetization. The values obtained at 300 K are 525, 347 and 126 mT for the starting Co-NRs, the **Co-P$_{0.2/165}$** NRs and the **Co-P$_{0.7/165}$** NRs, respectively. This change is attributed to a fragmentation of the hcp Co core, which is corroborated by the TEM observations for the sample **Co-P$_{0.7/165}$** (Fig. 1b and 2c). The Co core cannot be considered as a continuous cylinder anymore, thus,

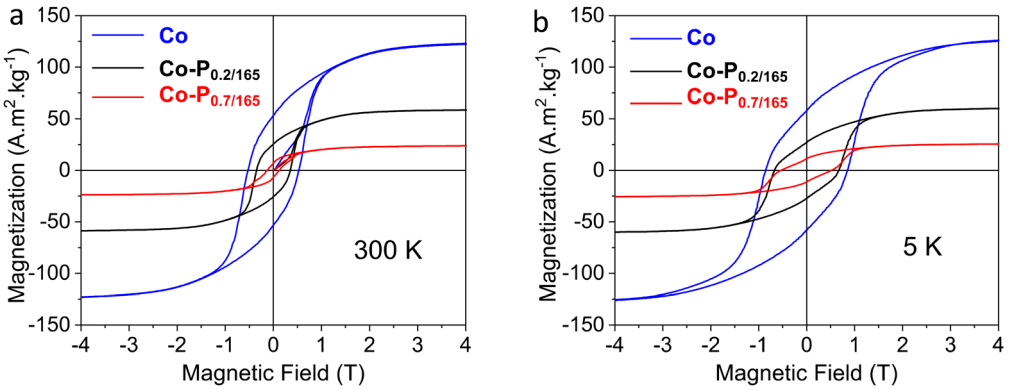

Fig. 3 Magnetization curves at (a) 300 K and (b) 5 K of the initial Co-NRs (blue), the **Co-P$_{0.2/165}$** NRs (black) and the **Co-P$_{0.7/165}$** NRs (red).

the contribution of shape magnetic anisotropy to coercivity is reduced. While the TEM images are less conclusive for the **Co-P$_{0.2/165}$** sample, the decrease in the H_c value leads to the same conclusion, albeit to a lesser extent. For both samples, the cycles at 5 K (Fig. 3b) do not present any exchange bias in any sample, which is in agreement with the absence of any significant amount of CoO in contact with metallic Co.

In order to understand whether the incomplete transformation can be attributed to a too low reaction temperature (165 °C) or to an insufficient PTMS amount, we performed two control reactions, allowing them to proceed for a longer period (3 h). The first reaction, leading to **Co-P$_{0.5/250}$** (Table S2† entry 4), was performed using a Co/P ratio of 1/0.5 but increasing the temperature to 250 °C. As the mesitylene boiling point did not allow for reaching this temperature, the experiment was performed in oleylamine. The second reaction, leading to **Co-P$_{3/165}$**, (Table S2† entry 5) was performed at 165 °C with a Co/P ratio of 1/3. The TEM analyses of **Co-P$_{0.5/250}$** and **Co-P$_{3/165}$** NRs are shown in Fig. 4a and 5a respectively. While both samples retain their anisotropic shape, most of the **Co$_{0.5/250}$** NRs are bent and present irregular thickness or enlarged tips. EDX line analysis of two NRs shows that they both contain both Co and P (Fig. S3†). The HRTEM analyses of **Co-P$_{0.5/250}$** and **Co-P$_{3/165}$**, are presented in Fig. 4b and 5b, respectively. The two areas analyzed in **Co-P$_{0.5/250}$** (Fig. 4b) correspond to two different NRs. We identified a different phase for each NR: orthorhombic Co_2P in the area framed in yellow (Fig. 4b and c) and hcp Co for the area framed in cyan (Fig. 4b and d). On the other hand, **Co-P$_{3/165}$** presents a more homogeneous aspect (Fig. 5a) and the NRs examined showed only the presence of crystallized orthorhombic Co_2P (Fig. 5b). Both **Co-P$_{0.5/250}$** and **Co-P$_{3/165}$**, are polycrystalline, as evidenced by the HRTEM images presented in Fig. S4 and S5,† respectively.

The XRD patterns of the **Co-P$_{0.5/250}$** and **Co-P$_{3/165}$** NRs show the presence of both Co_2P and hcp Co (Fig. 6a). For **Co-P$_{3/165}$**, the peaks associated to the hcp Co are less intense. This is in agreement with the magnetic measurements (Fig. 6b and Table S2†) that reveal M_s values of 10.2 A m^2 kg^{-1} and 3.3 A m^2 kg^{-1} for the **Co-P$_{0.5/250}$** and **Co-P$_{3/165}$** NRs, respectively. These values correspond to 6.4 wt% and 2.1 Co wt%, respectively. For comparison, the starting Co-NRs present an M_s value of 134 A m^2 kg^{-1}. This indicates that when P is in large excess, even at low temperatures, homogeneous and quasi-complete transformation of the Co to Co_2P can be achieved. On the other hand, under stoichiometric conditions, it is more difficult to transform completely Co into Co_2P even at high temperature. The degree of phosphidization of the different experiments is summarized in Table S2.†

Interestingly, performing the reaction at 250 °C for 3 h and with a Co/P ratio of 1/3 (**Co-P$_{3/250}$**) allows almost complete transformation of Co into CoP. TEM, XRD and magnetic measurements of the **Co-P$_{3/250}$** NRs are presented in Fig. 7. TEM images of **Co-P$_{3/250}$** NRs show conservation of the anisotropic shape without contrast differences (Fig. 7a). In Fig. 7b we present an NR array with the long NR axes oriented perpendicularly with respect to the TEM-grid plane. Similar self-organized superlattices have been regularly observed during the synthesis of the starting Co nanorods.[63] The XRD diffractogram (Fig. 7c) shows only the presence of a well-crystallized CoP phase. The low magnetization and coercivity (Fig. 7d and Table S2† entry 6) can be attributed to metallic Co residues (less than 2 wt% of Co(0)). In Fig. S6† we present the EDX line analysis on a **Co-P$_{3/250}$** NR array with the long NR axes oriented perpendicularly with respect to the TEM-grid plane. As expected for an almost complete conversion to CoP, no core@shell structure was observed in contrast to the **Co-P$_{0.7/165}$** sample (Fig. 2). Due to the lower density of CoP and Co_2P as compared to Co (ρ_{Co} = 8.90 g cm^{-3}; ρ_{Co_2P} = 7.54 g cm^{-3}; ρ_{CoP} = 6.42 g cm^{-3}), the chemical transformation to Co_2P and CoP leads to an expansion of the nanorod volume, which is well-illustrated by an increase in the diameters of the phosphidized nanorods measured by TEM (Table S1†).

In order to investigate the crystallinity of the nanorods, HRTEM analyses have been performed on several specimens. In agreement with XRD, the HRTEM and FFT analyses (Fig. 8) revealed only the presence of crystallites of the orthorhombic CoP phase but in different zone axes. The NRs appear polycrystalline and no growth axis was identified. The HRTEM micrographs of several specimens of the nanorod array exhibit Moiré fringes which strongly supports the polycrystalline struc-

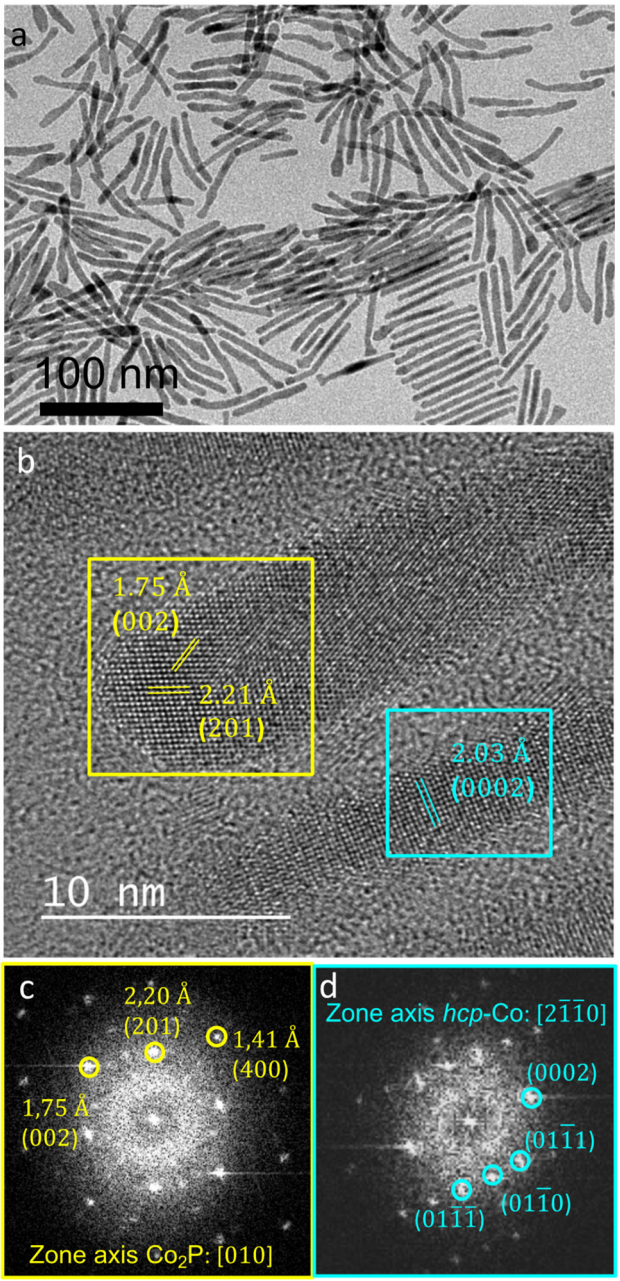

Fig. 4 **Co-P$_{0.5/250}$**: (a) (TEM), (b) HRTEM of two specimens; (c) and (d) FFT of the areas presented in (b), in yellow and cyan frames, respectively. The image zone-axis and the corresponding spots identification are indicated in the figure. The yellow and cyan-framed areas correspond to Co_2P and hcp Co, respectively.

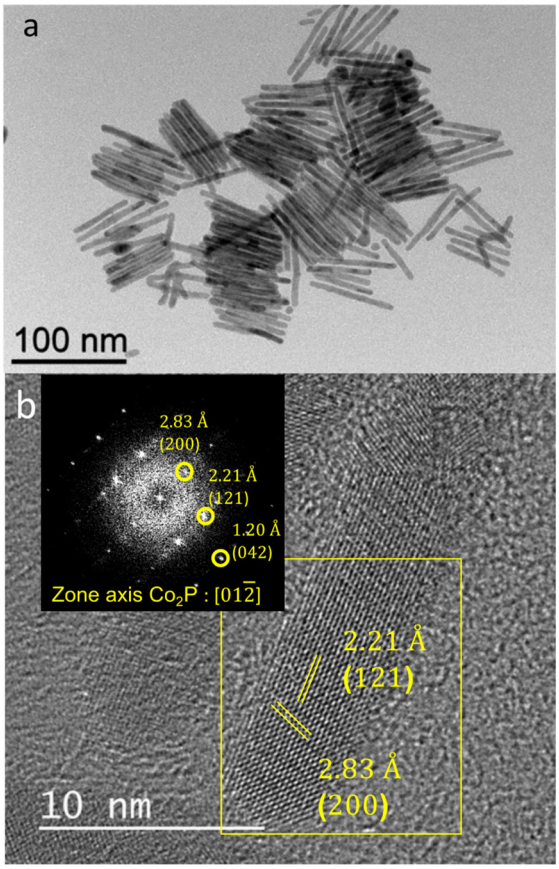

Fig. 5 (a) TEM image and (b) HRTEM image of a **Co-P$_{3/165}$** sample. The inset in (b) shows the FFT obtained from the yellow-framed area. The spots in the FFT have been indexed and are in agreement with the Co_2P bulk structure.

ture for the **Co-P$_{3/250}$** NRs. The absence of preferential growth direction and the polycrystallinity of the CoP NRs was confirmed by the Rietveld analysis of the XRD pattern. In Table S3† the coherence length/crystallite sizes for the main (*hkl*) reflections of CoP are reported. They are almost identical and close to the diameter of the rods.

Our results indicate that phosphidization yields, expressed as % of Co converted either into Co_2P or CoP, depend both on the temperature and the P/Co ratio. From Table S2,† we can make the following observations: at 165 °C, 0.2 eq. of P (entry 2) is enough to bring about the expected transformation into Co_2P, however, an over-stoichiometric ratio (entry 3) does not achieve the complete transformation into Co_2P. Transformation of Co into Co_2P at this temperature progressed to 96.6% with an excess of P and by prolongation of the reaction (entry 5). This is most likely due to the inward diffusion of P being more favorable at the initial transformation steps. A Co/ratio of 3 at 165 °C (entry 5) seems to be more efficient in transforming Co into Co_2P than a stoichiometric 0.5 ratio at 250 °C (entry 4). This indicates that a high P concentration favors the Co to Co_2P transformation more than high temperature. Nevertheless, both P excess and high temperature are necessary to transform Co into CoP (entry 6). While, no coexistence of Co_2P and CoP has been evidenced in any of the samples, we cannot exclude the presence of non-identified amorphous phases during the transformations. It has been postulated[22] that the transformation of Co to Co_2P initially proceeds by diffusion of P into the Co lattice, and when Co_2P becomes majority, by diffusion of Co into the Co_2P lattice, with a concomitant formation of voids due to the Kirkendall

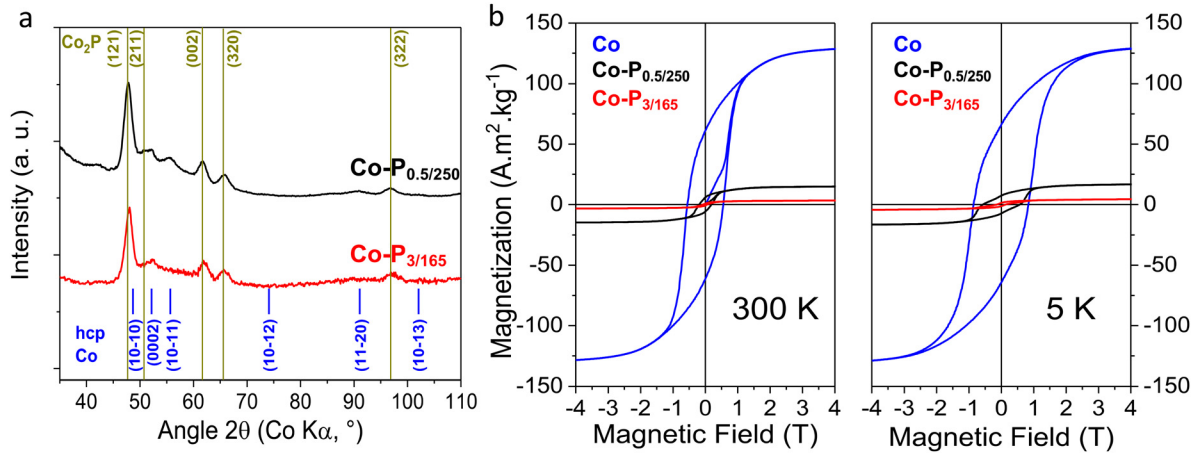

Fig. 6 (a) XRD diffractograms of **Co-P$_{0.5/250}$** and **Co-P$_{3/165}$**; blue and olive green lines correspond to the expected reflections of hcp-Co (COD file 9008492, *P*63/*mmc*, *a* = 2.507 Å, *c* = 4.068 Å) and orthorhombic Co_2P (COD file 9009202, *Pnam*, *a* = 5.646 Å, *b* = 6.608 Å, *c* = 3.513 Å) and (b) magnetization curves at 300 K and 5 K of starting Co nanorods (blue), **Co-P$_{0.5/250}$** (black) and **Co-P$_{3/165}$** (red).

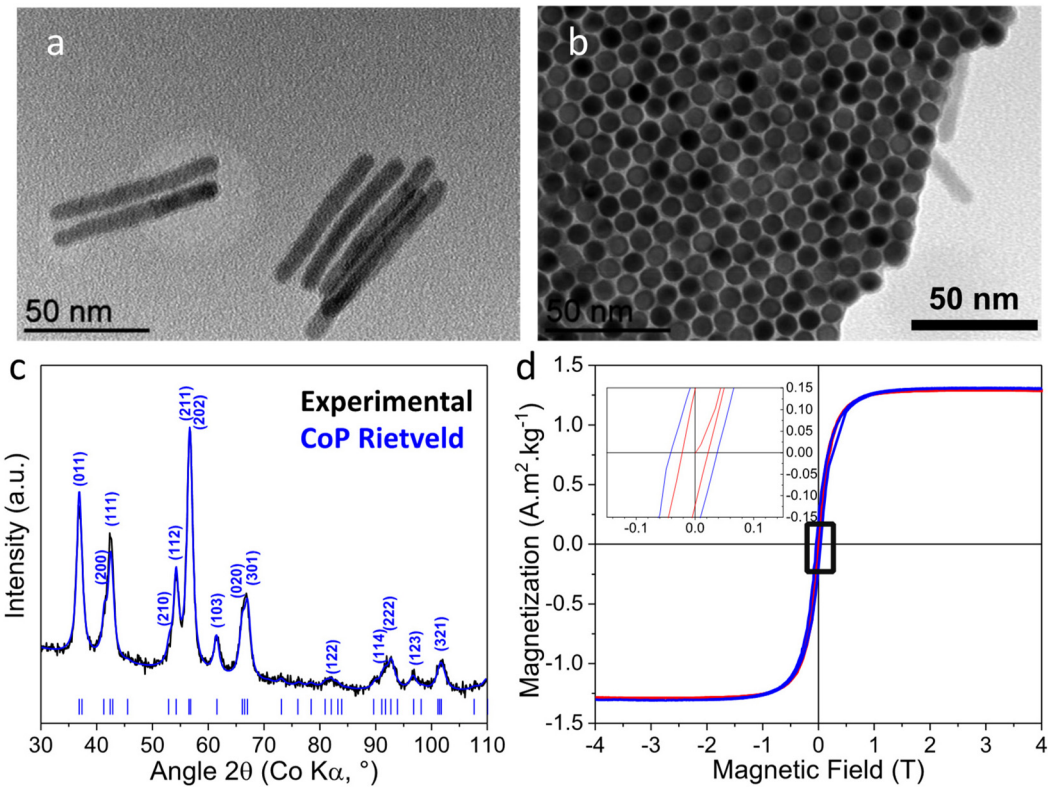

Fig. 7 **Co-P$_{3/250}$** (a) TEM of NRs lying flat on the TEM grid (b) top view TEM of an NR array with the long NR axes oriented parallel to the electron beam; (c) XRD and Rietveld analysis (R_{wp} = 2.2%) of the CoP phase (COD file 9008928, *Pnma*, *a* = 5.076 Å, *b* = 3.281 Å, *c* = 5.599 Å) indexed with the most intense reflections for the given peak; (d) magnetization curves at 300 K (red) and 5 K (blue). The inset shows enlargement of the low-field area revealing a weak coercive field (5 K: 39 mT, 300 K: 22 mT).

effect. Further transformation of Co_2P into CoP, occurs by diffusion of Co in the lattice, the anion that theoretically should remain intact, but in practice accentuates the voids. In our case, no voids were detected in any of our phosphidized NRs.

The availability of cobalt phosphide-based NRs of different configurations/compositions incited us to explore their performances in the selective hydrogenation of PhA. In addition to the inorganic phosphorous ligand effect discussed in the introduction section, reported studies have shown that the

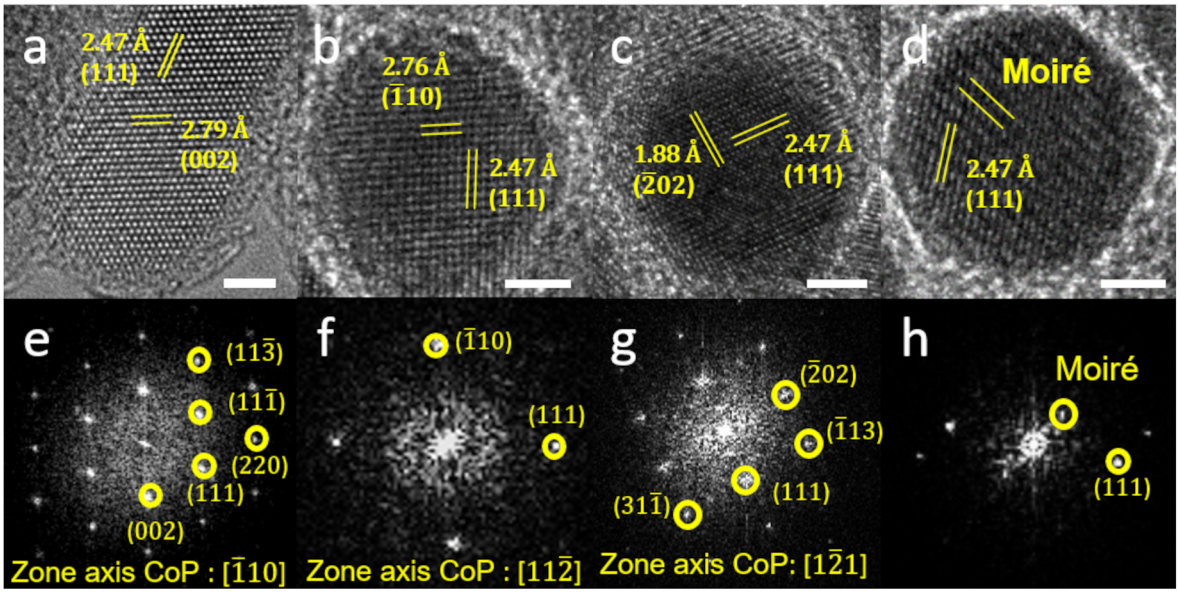

Fig. 8 **Co-P$_{3/250}$** HRTEM (a–d) and the corresponding FFT (e–f) of different NRs: (a and e) an NR lying flat on the grid, and (b–d and f–h) different NRs of an array of NRs oriented perpendicularly to the TEM-grid and the electron beam (scale-bars = 2 nm).

catalytic performance of metal phosphide catalysts is affected by their structure and their composition, including the crystal facet, exposed termination, metal type and metal/P ratio. For Al_2O_3-supported Ni phosphide catalysts, it has been shown that the catalytic activity (100 °C, 3 bar H_2) decreases gradually along with the decrease of the Ni/P ratio, the higher activity obtained for Ni/Al_2O_3 (8.25 mol_{PhA} mol_{Ni}^{-1} h^{-1}).[60] This might be tentatively attributed to a slower H_2 activation rate by heterolytic dissociation on the Ni phosphide catalysts as compared to a homolytic dissociation on the metallic particles.[69,70] However, with the gradual incorporation of P, the selectivity toward ST increases dramatically from 0.7% for Ni/Al_2O_3 to a maximum of 88.2% on Ni_2P/Al_2O_3, followed by a decrease to 65.9% for NiP_2/Al_2O_3. The enhanced selectivity was attributed to: (i) the fact that the incorporation of P increases the Ni–Ni bond length, which modifies the alkene adsorption (from di-σ to π coordination), and (ii) the reduced electron density of Ni sites ($Ni^{\delta+}$), which contributes to decreasing the desorption energy of the alkene. For unsupported $Co_{1.2}P$ catalysts, a modest activity of 0.03 mol_{PhA} mol_{Co}^{-1} h^{-1} was measured (100 °C, 7 bar H_2) with a high ST selectivity of 95%.[24] A higher activity (0.625 mol_{PhA} mol_{Co}^{-1} h^{-1}) was reported for a Co_2P catalyst modified by the addition of tri-*n*-butylphosphine.[71]

Our investigation focused first on the **Co-P$_{0.2/165}$** and **Co-P$_{0.7/165}$** NRs. Apart from the ICP and VSM analyses, XPS analyses were also performed on the NRs tested in catalysis (Table S4†). As expected, the Co/P ratio was higher for the **Co-P$_{0.2/165}$** NRs (Co/P = 2.2) than for the **Co-P$_{0.7/165}$** NRs (Co/P = 1.2). The electronic states of Co and P were probed by XPS, since electron transfer from Co to P could be expected. Indeed, XPS data on cobalt phosphide report Co $2p_{3/2}$ binding energy (BE) of 779–779.6 eV for CoP[69,72] and 778.2 eV for Co_2P.[29,73] These BEs shift positively from that of metallic Co-NRs (777.9 eV).[74] The Co $2p_{3/2}$ BE of CoP is higher than that of Co_2P and metallic Co, indicating that a higher phosphorus content causes an electron density shift from Co to P due to the higher electronegativity of phosphorus. In the case of Co_2P, the Co $2p_{3/2}$ binding energy is very close to that of metallic Co, suggesting a relatively low positive charge on cobalt for this phosphide ($Co^{\delta+}$, $\delta < 1$), as predicted by DFT calculations (0.17 e^-).[75] Two pairs of peaks can be observed in the high-resolution Co 2p spectra of the cobalt phosphide comprising NRs (Fig. S7a and b†). The first pair of peaks at ~778 eV and ~793 eV corresponds to binding energies (BE) close to that of metallic cobalt, as expected for Co_2P. The higher BE measured for the **Co-P$_{0.7/165}$** NRs (Co $2p_{3/2}$ 778.2 eV) compared to the **Co-P$_{0.2/165}$** NRs (778.0 eV) should be related to a thicker layer of cobalt phosphide that seems to cover more efficiently the remaining Co^0. The second pair of peaks at BE ~780 eV and ~796.5 eV can be assigned to surface cobalt oxidation, and could correspond to $Co(OH)_2$.[76] Interestingly, the ratio between non-oxidized and oxidized cobalt is higher for the **Co-P$_{0.7/165}$** NRs (Table S4†), suggesting that a thicker Co_2P layer constitutes better protection towards air oxidation upon exposure to the air. For the deconvoluted P 2p spectra (Fig. S7d and e†), the two peaks centered at 129.3 eV and 130.2 eV corresponding to the P $2p_{3/2}$ and P $2p_{1/2}$ are assigned to P with a partial negative charge, characteristic of phosphides,[77] while the peak located at 132.3 eV is ascribed to oxidized phosphorus species arising from surface oxidation of the air-exposed NRs.[78]

Supported, as well as free standing **Co-P$_{0.2/165}$** and **Co-P$_{0.7/165}$** NRs were tested for the selective hydrogenation of PhA and compared to bare Co-NRs. The selective hydrogenation of

PhA was first performed at 90 °C under 5 bar of H_2 in methanol. In the first series of experiments, the performances of bare Co, **Co-P$_{0.2/165}$** and **Co-P$_{0.7/165}$** NRs that were supported on oxidized few-layer graphene (FLG, 50 m^2 g^{-1}) were compared. This carbon support was used because: (i) its two-dimensional morphology should favor Co-NR deposition and stabilization, (ii) carbon supports are very commonly used in hydrogenation reactions, and (iii) oxidized carbon supports can favor hydrogen spillover (H-spillover), which can be involved in hydrogenation reactions.[79] TEM micrographs of these three catalysts (5% Co w/w) are shown in Fig. S8.† All NRs were well dispersed on the FLG support. As shown in Fig. 9a, the space time yields (STY, mol_{PhA} mol_{Co}^{-1} h^{-1}) of the three samples are quite similar at around 30 mol_{PhA} mol_{Co}^{-1} h^{-1} affording up to 90% conversion. This result does not support a reduced surface concentration of the H atom on the supported **Co-P$_{0.2/165}$** and **Co-P$_{0.7/165}$** NRs as compared to the hcp-Co,[60] for which facile H_2 dissociation has been reported.[80] As far as selectivity is concerned, three products are formed: ST, EB and toluene. The production of toluene, a product of alkylation in the side chain during PhA hydrogenation, has already been reported for Ni catalysts modified with Keggin-type heteropoly compounds.[81] In that work, the production of toluene was attributed to the acidity of the Keggin-type compound that favors the

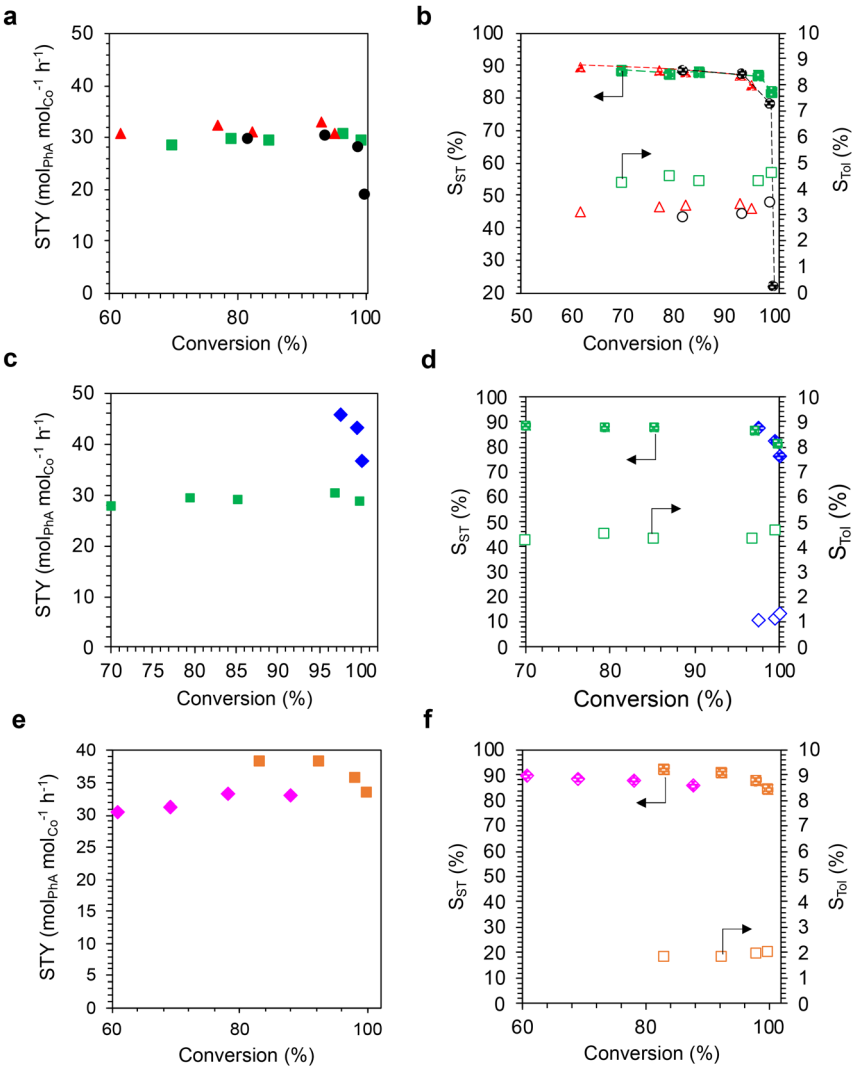

Fig. 9 (a) STY *versus* conversion curves for PhA hydrogenation on the FLG supported Co-NR catalysts. (b) Conversion *versus* selectivity curves for PhA hydrogenation on the FLG supported Co-NR catalysts. Black circles represent bare **Co/FLG**, red triangles represent **Co-P$_{0.2/165}$/FLG**, and green squares represent **Co-P$_{0.7/165}$/FLG**. (c) STY *versus* conversion curves for PhA hydrogenation on the **Co-P$_{0.7/165}$/FLG** catalyst without and with water. Green squares represent **Co-P$_{0.7/165}$/FLG** without water and blue diamonds represent **Co-P$_{0.7/165}$/FLG** with water. (d) Conversion *versus* selectivity curves for PhA hydrogenation on the **Co-P$_{0.7/165}$/FLG** catalyst without and with water. Green squares represent **Co-P$_{0.7/165}$/FLG** without water and blue diamonds represent **Co-P$_{0.7/165}$/FLG** with water. (e) STY *versus* conversion curves for PhA hydrogenation on the **Co-P$_{0.7/165}$/TiO$_2$** catalyst without and with water. (f) Conversion *versus* selectivity curves for PhA hydrogenation on the **Co-P$_{0.7/165}$/TiO$_2$** catalyst without and with water. Orange squares represent **Co-P$_{0.7/165}$/TiO$_2$** without water, and cyan diamonds represent **Co-P$_{0.7/165}$/TiO$_2$** with water. Conditions: PhA/Rh = 500, 90 °C, 5 bar H_2, 6 h, methanol.

alkylation reaction. As the FLG support was oxidized with nitric acid, it contained significant amounts of carboxylic groups on its surface.[82] We have independently evaluated the performance of unsupported Co-NRs and checked for the presence of toluene. In that case, no toluene was formed (Fig. S9†). Consequently, it is reasonable to propose that toluene (3–5% for all supported Co-NR catalysts) was formed because of the acidity of the FLG support. Fig. 9b shows the evolution of selectivity towards ST and toluene with conversion for the three catalysts. The selectivity towards ST remains very high (82.6%) at 99.6% conversion for the **Co-P$_{0.7/165}$/FLG**, while it drops to 22% at 100% conversion for the **Co/FLG** catalyst. At a lower conversion (90%), the three catalysts behaved similarly, showing an $S_{ST\text{-}90\%}$ of 87%.

As **Co-P$_{0.7/165}$/FLG**, was the most interesting catalyst as far as the activity and selectivity to ST are concerned, the possibility to improve its performances was explored. The use of water as a promoter was first investigated. The positive role of water to enhance activity and selectivity in hydrogenation reactions has been attributed to water-involved hydrogen exchange[83,84] and H-spillover.[85] It has been shown that H-spillover can result in an enhanced activity in PhA hydrogenation.[86–88] It is also known that gas phase H-spillover on carbon support can be enhanced by the presence of water, which acts as a shuttle for the spilt-over hydrogen species.[89] Color change originating from the reduction of WO_3 is considered as a simple verification method of H-spillover.[89]

The occurrence in the liquid phase of H-spillover was evaluated for the **Co-P$_{0.7/165}$/FLG** catalyst in the presence or absence of water. To directly monitor the H-spillover in the liquid phase, the reduction behavior of WO_3 in the presence or absence of the catalyst was followed under the same conditions where PhA hydrogenation was conducted (90 °C, 5 bar H_2, methanol in batch reactor). Under these experimental conditions, no H-spillover was detected for the **Co-P$_{0.7/165}$/FLG** sample after 30 min, as shown from the identical color of the samples before and after catalysis, either in the presence of absence of water (Fig. S10a†). A PhA hydrogenation test was performed on the **Co-P$_{0.7/165}$/FLG** catalyst in the presence of 1 mL of water. Under these conditions, the catalyst is more active (Fig. 9c), exhibiting an STY of ~45 mol_{PhA} mol_{Co}^{-1} h^{-1} (30 mol_{PhA} mol_{Co}^{-1} h^{-1} in the absence of water). Interestingly this catalyst also shows a selectivity towards ST of 76.7% at 100% conversion and a significantly lower selectivity towards toluene than in the case of the reaction performed without water addition (Fig. 9d). As H-spillover seems not to be operative with this catalyst, it is possible that water contributes to the hydrogenation of PhA by acting as a hydrogen donor.[90]

Another strategy to modulate the catalytic performance is to change the support. The use of TiO_2, a reducible support allowing H-spillover, which has already shown interesting performance as a support for PhA hydrogenation[91] was investigated. With such an oxide support, different metal–support interactions as compared to the carbon support can be expected, which can impact catalytic performances.[92,93] The **Co-P$_{0.7/165}$** NRs were supported on a commercial $TiO_{2\text{-}P25}$ support (BET surface area 57 m^2 g^{-1}), which consists of a mixture of 78% anatase and 22% rutile TiO_2. Representative TEM micrographs of the **Co-P$_{0.7/165}$/TiO$_2$** catalyst are shown in Fig. S11a.† The **Co-P$_{0.7/165}$/TiO$_2$** catalyst shows a high STY (~38 mol_{PhA} mol_{Co}^{-1} h^{-1}, Fig. 9e) and a selectivity towards ST of 83.9% at 100% PhA conversion (Fig. 9f). The selectivity towards toluene was lower on TiO_2 (~2%) than on FLG (~4.5%). Both Lewis and Brønsted acid sites, which could be responsible for the formation of toluene are present on $TiO_{2\text{-}P25}$.[94] H-spillover also operates on TiO_2,[95] and water-assisted proton diffusion on oxide surface is a known phenomenon.[96,97] The surface H_3O^+ species can contribute to the reaction by decreasing the energy barrier of PhA hydrogenation.[98] We have also evaluated the occurrence of H-spillover on the **Co-P$_{0.7/165}$/TiO$_2$** catalyst in the presence or absence of water, and no H-spillover was detected (Fig. S10b†). The reactivity of the **Co-P$_{0.7/165}$/TiO$_2$** catalyst was investigated in the presence of 1 mL of water (Fig. 9e and f). In the presence of water, the **Co-P$_{0.7/165}$/TiO$_2$** catalyst is less active (Fig. 9e) and shows similar selectivity as when water is absent from the medium (Fig. 9f). As for the **Co-P$_{0.7/165}$/FLG** catalyst, the presence of water has a negative impact on toluene formation, since no toluene was formed for the P$_{0.7/165}$/TiO$_2$ catalyst in the presence of water.

From this first series of experiments, we can conclude first that, compared to the Co-NRs and **Co-P$_{0.2/165}$** NRs, the **Co-P$_{0.7/165}$** NRs show the best compromise between activity and selectivity. Second, the tests carried out to optimize this system by playing with the nature of the support and/or the presence of water in the medium allowed us to identify the system "**Co-P$_{0.7/165}$**/TiO$_2$ without water in the medium" as the most interesting in terms of activity and selectivity (Fig. S12†).

In contrast to the **Co-P$_{0.2/165}$** and **Co-P$_{0.7/165}$** NRs that present Co_2P on their surface, the **Co-P$_{3/250}$** NRs are composed almost exclusively of CoP (Table S2†). As the literature points to the influence of the modulation of the Co/P ratio on catalytic performances, the **Co-P$_{3/250}$** NRs supported on FLG were compared with FLG-supported **Co-P$_{0.2/165}$** and **Co-P$_{0.7/165}$** NRs.

As expected, the Co/P surface ratio is lower for the **Co-P$_{3/250}$** NRs than for the **Co-P$_{0.2/165}$** and **Co-P$_{0.7/165}$** NRs (Table S4†). The XPS Co 2p spectrum of **Co-P$_{3/250}$** NRs presents a single pair of peaks with BEs at 778.6 and 793.6 eV (Fig. S7c†). Contrary to the **Co-P$_{0.2/165}$** and **Co-P$_{0.7/165}$** NRs, the **Co-P$_{3/250}$** NRs do not show significant cobalt surface oxidation. This is expected, since only traces of oxidizable Co(0) is present in the **Co-P$_{3/250}$** NRs (Table S2†); and in addition, this Co(0) is most likely not on the surface, thus, protected by CoP. In Fig. 10a, the XPS-derived evolution of the Co(0)/CoO_x ratio as a function of the Co/P atomic ratio is presented for the three types on NRs. For the P 2p spectrum (Fig. S8f†), the two peaks centered at 129.3 eV and 130.4 eV corresponding to P $2p_{3/2}$ and P $2p_{1/2}$ are well assigned to P with a partial negative charge of phosphides, while the peaks located at 132.8 and 134.9 eV correspond to the phosphate due to surface oxidation. These values are in good agreement with those reported for CoP nanorods.[41]

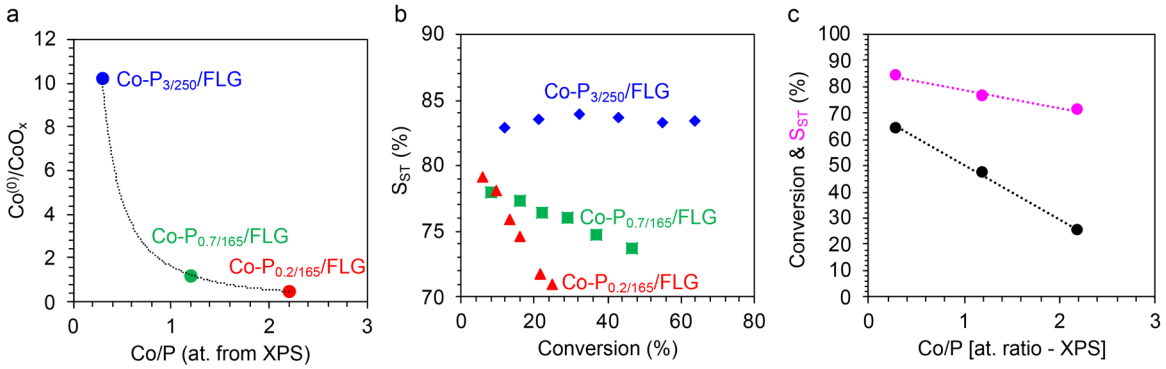

Fig. 10 (a) Evolution of the $Co_{non-oxidized}/Co_{oxidized}$ ratio determined by XPS with the atomic Co/P ratio determined by XPS. (b) STY *versus* conversion curves for PhA hydrogenation on **Co-P$_{0.2/165}$/FLG** (red triangles), **Co-P$_{0.7/165}$/FLG** (green squares), and **Co-P$_{3/250}$/FLG** (blue diamonds) catalysts. (c) Correlation between the Co/P atomic ratio determined by XPS and the PhA conversion (for a 6 hours-test, black circles) and S_{ST} determined at 25% conversion (purple circles). Conditions: PhA/Rh = 500, 100 °C, 5 bar H_2, 6 h, methanol.

This suggests that the Co atoms in the **Co-P$_{3/250}$** NRs have a partial positive charge ($Co^{\delta+}$), while the P atoms have a partial negative charge, implying the transfer of electron density from Co to P.

As the differences in activity and selectivity between the **Co-P$_{0.2/165}$/FLG** and **Co-P$_{0.7/165}$/FLG** catalysts were not marked at 90 °C (Fig. 9a and b), we performed a new series of tests including also FLG-supported **Co-P$_{3/250}$** NRs at 100 °C under 5 bar of H_2 in methanol. The performances of the **Co-P$_{0.2/165}$/FLG**, **Co-P$_{0.7/165}$/FLG**, and **Co-P$_{3/250}$/FLG** catalysts during these 6 hours-tests are presented in Fig. 10b. The **Co-P$_{3/250}$/FLG** catalyst shows the best performance both in terms of conversion and selectivity. In fact, linear correlations were found between the Co/P ratio and the catalytic performances (Fig. 10c). The superior performance of the **Co-P$_{3/250}$/FLG** catalyst in terms of activity could be rationalized by a favored H_2 dissociation on CoP. Experimental results have shown that treatment of CoP with H_2 introduced large amounts of reactive hydrogen onto CoP, of the order of one H per Co or the P surface atom.[62] The improved performance of the **Co-P$_{3/250}$/FLG** catalyst in terms of selectivity could be due to the reduced electron density of Co sites ($Co^{\delta+}$), which should contribute to decreasing the ST desorption energy. Considering the promising performances of the **Co-P$_{3/250}$** NRs, they were also supported on TiO_2 (Fig. S11b† for a representative TEM micrograph). We have evaluated the occurrence of H-spillover on the **Co-P$_{3/250}$/TiO$_2$** catalyst in the presence or absence of water (Fig. S10c†). Without water in the reaction medium, H-spillover was operative for this sample, as the color of the solution containing **Co-P$_{3/250}$/TiO$_2$** and WO_3 changed (WO_{3-x}), indicating that the reduction of WO_3 was promoted at 100 °C by the H-spillover in the liquid phase. This result also suggests a favored H_2 dissociation on **Co-P$_{3/250}$** NRs as compared to **Co-P$_{0.7/165}$** NRs. In the presence of water, no H-spillover was observed, which could be related to the surface oxidation of the **Co-P$_{3/250}$** NRs at 100 °C in water or to the formation of a thin water layer of H_2O molecules preferentially adsorbed on the surface of the catalyst.[69] The **Co-P$_{3/250}$/TiO$_2$** catalyst was evaluated for PhA hydrogenation in the presence or absence of 1 mL of water (Fig. S13†). Either in the presence of water or in its absence, this catalyst was less active but more selective than the **Co-P$_{3/250}$/FLG** catalyst. In this case, the presence of water did not affect much the catalyst performances. The **Co-P$_{3/250}$/TiO$_2$** catalyst shows an $STY_{20\%}$ of ~20 mol_{PhA} mol_{Co}^{-1} h^{-1} ($STY_{20\%}$ of ~41 mol_{PhA} mol_{Co}^{-1} h^{-1} for the **Co-P$_{3/250}$/FLG** catalyst, Fig. S12a†) and an $S_{ST\text{-}20\%}$ of 93% ($S_{ST\text{-}20\%}$ of 83% for the **Co-P$_{3/250}$/FLG** catalyst, Fig. S12b†).

Considering the superior performances of the **Co-P$_{3/250}$/FLG** and **Co-P$_{3/250}$/TiO$_2$** catalysts in terms of activity and selectivity, their stability was also evaluated through three recyclability tests. These tests were performed at low PhA conversions, typically less than 15%. As shown in Fig. S14,† the catalysts show quite good stability. TEM analyses were also performed on fresh and post-catalysis catalysts. The micrographs presented in Fig. S15† confirm the stability of these catalysts, nanorods retaining their integrity after catalysis.

While detailed mechanistic investigations and structure/property correlations deserve a dedicated exploration and are beyond the scope of this work, several important elements emerge from this preliminary study on the catalytic properties for semi-hydrogenation of PhA of the cobalt phosphide nanorods prepared. First, a number of parameters allowing to modulate the activity and selectivity of these catalysts have been identified, such as: (i) the Co/P ratio in the nanorods, which plays a key role on the catalytic performances and the resistance towards oxidation; (ii) the presence of a support whose acidic properties must be controlled to avoid the formation of toluene; and (iii) the presence of water in the medium, which can in some cases be beneficial both for the activity and the selectivity.

The prepared catalysts exhibit very promising catalytic performances, particularly in comparison with the results reported in the literature for the selective hydrogenation of PhA on Ni or Co phosphide catalysts (Table S5†).

4. Conclusions

The topochemical reaction of PTMS with metallic Co-NRs can be controlled to afford Co@Co_2P core@shell NRs of tunable shell thickness, or even CoP nanorods, depending on the reaction conditions employed. The Co@Co_2P nanorods present magnetic properties stemming from their ferromagnetic Co core. As the phosphidization reaction transforms a part of the ferromagnetic Co core to the non-magnetic Co_2P and CoP phases, the magnetic properties can be modulated through the extent of phosphidization. No Kirkendall effect has been evidenced in any of the phosphidized samples, which is surprising considering the transformation mechanism proposed in the literature.[22]

The supported Co@Co_2P and CoP NRs are very promising catalysts for the selective hydrogenation of phenylacetylene to styrene, outperforming most Ni and Co phosphide catalysts reported in the literature, with supported CoP being the most active and selective catalyst. Finally, thanks to their magnetic core, the Co@Co_2P NRs should present the advantage of an easy recovery, and last but not least, the possibility to be used in catalytic reactions induced by magnetic heating.[99] In this context, we are confident that this strategy can be applied to shape-controlled nanoparticles of magnetic metals and alloys allowing tailoring their magnetic and catalytic properties.

Author contributions

Brandon Azeredo: investigation, data curation, formal analysis, and writing original draft. Jason Nguyen-Cong: investigation, data curation, and formal analysis. Mathieu Vidal: investigation, data curation, and writing original draft. Seema Shafiq, Thi Thiet Vu, Beatrice Muzzi, Audrey Marty, Yuanyuan Min, and Fabio Ferrari: investigation and data curation. Fabien Delpech and Céline Nayral: supervision and writing – review & editing. Pier-Francesco Fazzini and Thomas Blon: formal analysis and writing – review & editing. Philippe Serp, Guillaume Viau, and Katerina Soulantica: project administration, funding acquisition, supervision, methodology, formal analysis, and writing – review & editing.

Data availability

The data supporting this article have been included as part of the ESI.†

Conflicts of interest

The authors declare no competing financial interest.

Acknowledgements

The authors thank the European Union's Horizon 2020 research and innovation program for financial support of the SWIMMOT project under grant agreement no. 899612. This project has received funding from the French ANR national call (Project NIMRod ANR-21-CE09-0019). This work has received funding from the French Agence Nationale de la Recherche under grant agreements ANR-21-CE07-0021 (GRAAL) and ANR-22-CE07-0044 (LICORN).

References

1 S. T. Oyama, T. Gott, H. Zhao and Y.-K. Lee, *Catal. Today*, 2009, **143**, 94–107.
2 S. T. Oyama, *J. Catal.*, 2003, **216**, 343–352.
3 R. Prins and M. E. Bussell, *Catal. Lett.*, 2012, **142**, 1413–1436.
4 J. F. Callejas, C. G. Read, C. W. Roske, N. S. Lewis and R. E. Schaak, *Chem. Mater.*, 2016, **28**, 6017–6044.
5 L. Chen, J.-T. Ren and Z.-Y. Yuan, *Green Chem.*, 2022, **24**, 713–747.
6 H. Yin, F. Rong and Y. Xie, *Int. J. Hydrogen Energy*, 2024, **52**, 350–375.
7 J. Cabana, L. Monconduit, D. Larcher and M. R. Palacín, *Adv. Mater.*, 2010, **22**, E170–E192.
8 B. Lan, Y. Wang, J. Lu, D. Liu, C. Wei, X. Zhang, X. Huang and G. Wen, *Particuology*, 2024, **88**, 11–31.
9 Y. Shi, M. Li, Y. Yu and B. Zhang, *Energy Environ. Sci.*, 2020, **13**, 4564–4582.
10 B. Liu, X. Lan, Q. Zhong and T. Wang, *ACS Catal.*, 2024, **14**, 757–775.
11 S.-H. Li, M.-Y. Qi, Z.-R. Tang and Y.-J. Xu, *Chem. Soc. Rev.*, 2021, **50**, 7539–7586.
12 S. Carenco, D. Portehault, C. Boissière, N. Mézailles and C. Sanchez, *Adv. Mater.*, 2014, **26**, 371–390.
13 F. Zaera, *Chem. Soc. Rev.*, 2013, **42**, 2746–2762.
14 Z. Pu, T. Liu, I. S. Amiinu, R. Cheng, P. Wang, C. Zhang, P. Ji, W. Hu, J. Liu and S. Mu, *Adv. Funct. Mater.*, 2020, **30**, 2004009.
15 S. L. Brock, S. C. Perera and K. L. Stamm, *Chem. – Eur. J.*, 2004, **10**, 3364–3371.
16 Y. Xia, Y. Xiong, B. Lim and S. E. Skrabalak, *Angew. Chem., Int. Ed.*, 2009, **48**, 60–103.
17 Y. Xie, H. L. Su, X. F. Qian, X. M. Liu and Y. T. Qian, *J. Solid State Chem.*, 2000, **149**, 88–91.
18 W. Maneeprakorn, M. A. Malik and P. O'Brien, *J. Mater. Chem.*, 2010, **20**, 2329.
19 L. Yi, P. Shao and Z. Wen, *New J. Chem.*, 2023, **47**, 9545–9549.
20 Y. Ni, J. Li, L. Zhang, S. Yang and X. Wei, *Mater. Res. Bull.*, 2009, **44**, 1166–1172.
21 H. Zhang, D.-H. Ha, R. Hovden, L. F. Kourkoutis and R. D. Robinson, *Nano Lett.*, 2011, **11**, 188–197.
22 D.-H. Ha, L. M. Moreau, C. R. Bealing, H. Zhang, R. G. Hennig and R. D. Robinson, *J. Mater. Chem.*, 2011, **21**, 11498.
23 L. Karam, C. Farès, C. Weidenthaler and C. N. Neumann, *Angew. Chem., Int. Ed.*, 2024, **63**, e202404292.

24 A. Ropp, R. F. André and S. Carenco, *ChemPlusChem*, 2023, **88**, e202300469.
25 J. Park, B. Koo, K. Y. Yoon, Y. Hwang, M. Kang, J.-G. Park and T. Hyeon, *J. Am. Chem. Soc.*, 2005, **127**, 8433–8440.
26 W. Yang, Y. Huang, J. Fan, Y. Yu, C. Yang and H. Li, *Nanoscale*, 2016, **8**, 4898–4902.
27 E. J. Popczun, C. G. Read, C. W. Roske, N. S. Lewis and R. E. Schaak, *Angew. Chem., Int. Ed.*, 2014, **53**, 5427–5430.
28 J. F. Callejas, C. G. Read, E. J. Popczun, J. M. McEnaney and R. E. Schaak, *Chem. Mater.*, 2015, **27**, 3769–3774.
29 Z. Huang, Z. Chen, Z. Chen, C. Lv, M. G. Humphrey and C. Zhang, *Nano Energy*, 2014, **9**, 373–382.
30 M. E. Mundy, D. Ung, N. L. Lai, E. P. Jahrman, G. T. Seidler and B. M. Cossairt, *Chem. Mater.*, 2018, **30**, 5373–5379.
31 A. Sodreau, H. G. Zahedi, R. Dervişoğlu, L. Kang, J. Menten, J. Zenner, N. Terefenko, S. DeBeer, T. Wiegand, A. Bordet and W. Leitner, *Adv. Mater.*, 2023, **35**, 2306621.
32 E. J. Popczun, C. W. Roske, C. G. Read, J. C. Crompton, J. M. McEnaney, J. F. Callejas, N. S. Lewis and R. E. Schaak, *J. Mater. Chem. A*, 2015, **3**, 5420–5425.
33 V. V. T. Doan-Nguyen, S. Zhang, E. B. Trigg, R. Agarwal, J. Li, D. Su, K. I. Winey and C. B. Murray, *ACS Nano*, 2015, **9**, 8108–8115.
34 T. Mitsudome, M. Sheng, A. Nakata, J. Yamasaki, T. Mizugaki and K. Jitsukawa, *Chem. Sci.*, 2020, **11**, 6682–6689.
35 M. Sheng, S. Fujita, S. Yamaguchi, J. Yamasaki, K. Nakajima, S. Yamazoe, T. Mizugaki and T. Mitsudome, *JACS Au*, 2021, **1**, 501–507.
36 J. Liu, M. Meyns, T. Zhang, J. Arbiol, A. Cabot and A. Shavel, *Chem. Mater.*, 2018, **30**, 1799–1807.
37 H. Hou, Q. Yang, C. Tan, G. Ji, B. Gu and Y. Xie, *Chem. Lett.*, 2004, **33**, 1272–1273.
38 Y. Ni, J. Li, L. Jin, J. Xia, J. Hong and K. Liao, *New J. Chem.*, 2009, **33**, 2055.
39 P. J. Thomas, P. Christian, S. Daniels, Y. Li, Y. S. Wang and P. O'Brien, *Pure Appl. Chem.*, 2006, **78**, 1651–1665.
40 Y. Li, M. A. Malik and P. O'Brien, *J. Am. Chem. Soc.*, 2005, **127**, 16020–16021.
41 Q.-Q. Sun, M. Wang, S.-J. Bao, Y. C. Wang and S. Gu, *Analyst*, 2015, **141**, 256–260.
42 K. Bhunia, M. Chandra, S. K. Sharma, D. Pradhan and S.-J. Kim, *Coord. Chem. Rev.*, 2023, **478**, 214956.
43 Y. Liu, C. Li, M. Yuan, X. Zhang, H. Lan, Y. Chen, M. Tian, K. Liu and L. Wang, *Catal. Sci. Technol.*, 2023, **13**, 3084–3093.
44 M. Sheng, S. Yamaguchi, A. Nakata, S. Yamazoe, K. Nakajima, J. Yamasaki, T. Mizugaki and T. Mitsudome, *ACS Sustainable Chem. Eng.*, 2021, **9**, 11238–11246.
45 H. Ishikawa, M. Sheng, A. Nakata, K. Nakajima, S. Yamazoe, J. Yamasaki, S. Yamaguchi, T. Mizugaki and T. Mitsudome, *ACS Catal.*, 2021, **11**, 750–757.
46 T. Vergunst, F. Kapteijn and J. A. Moulijn, *Ind. Eng. Chem. Res.*, 2001, **40**, 2801–2809.
47 S. Wang, T. Liu, Y. Zhu, X. Liu, Q. Luo, M. Zhu, T. Ding and T. Yao, *J. Phys. Chem. C*, 2023, **127**, 5911–5919.
48 X. Chen, A. Zhao, Z. Shao, C. Li, C. T. Williams and C. Liang, *J. Phys. Chem. C*, 2010, **114**, 16525–16533.
49 P. McNeice, M.-A. Müller, J. Medlock, W. Bonrath, N. Rockstroh, S. Bartling, H. Lund, K. Junge and M. Beller, *ACS Sustainable Chem. Eng.*, 2022, **10**, 9787–9797.
50 Q. Zhu, X. Lu, S. Ji, H. Li, J. Wang and Z. Li, *J. Catal.*, 2022, **405**, 499–507.
51 F. Chen, C. Kreyenschulte, J. Radnik, H. Lund, A.-E. Surkus, K. Junge and M. Beller, *ACS Catal.*, 2017, **7**, 1526–1532.
52 Q. Fan, S. He, L. Hao, X. Liu, Y. Zhu, S. Xu and F. Zhang, *Sci. Rep.*, 2017, **7**, 42172.
53 A. A. Shesterkina, O. A. Kirichenko, O. P. Tkachenko, A. L. Kustov and L. M. Kustov, *Nanomaterials*, 2023, **13**, 2247.
54 D. Albani, K. Karajovic, B. Tata, Q. Li, S. Mitchell, N. López and J. Pérez-Ramírez, *ChemCatChem*, 2019, **11**, 457–464.
55 D. Sharma, P. Choudhary, S. Kumar and V. Krishnan, *Small*, 2023, **19**, 2207053.
56 T. Mitsudome, *Catalysts*, 2024, **14**, 193.
57 X. Li, Y. Zhang, A. Wang, Y. Wang and Y. Hu, *Catal. Commun.*, 2010, **11**, 1129–1132.
58 W. Fu, L. Zhang, T. Tao and T. Tang, *J. Ind. Eng. Chem.*, 2021, **95**, 376–387.
59 S. Carenco, A. Leyva-Pérez, P. Concepción, C. Boissière, N. Mézailles, C. Sanchez and A. Corma, *Nano Today*, 2012, **7**, 21–28.
60 Y. Chen, C. Li, J. Zhou, S. Zhang, D. Rao, S. He, M. Wei, D. G. Evans and X. Duan, *ACS Catal.*, 2015, **5**, 5756–5765.
61 Z. Guo, Z. Wang and M. Zhang, *Chem. Eng. J.*, 2023, **463**, 142505.
62 M. F. Delley, Z. Wu, M. E. Mundy, D. Ung, B. M. Cossairt, H. Wang and J. M. Mayer, *J. Am. Chem. Soc.*, 2019, **141**, 15390–15402.
63 B. Cormary, T. Li, N. Liakakos, L. Peres, P.-F. Fazzini, T. Blon, M. Respaud, A. J. Kropf, B. Chaudret, J. T. Miller, E. A. Mader and K. Soulantica, *J. Am. Chem. Soc.*, 2016, **138**, 8422–8431.
64 L. Lutterotti, D. Chateigner, S. Ferrari and J. Ricote, *Thin Solid Films*, 2004, **450**, 34–41.
65 M. Vidal, J. Pandey, J. Navarro-Ruiz, J. Langlois, Y. Tison, T. Yoshii, K. Wakabayashi, H. Nishihara, A. I. Frenkel, E. Stavitski, M. Urrutigoïty, C. H. Campos, C. Godard, T. Placke, I. del Rosal, I. C. Gerber, V. Petkov and P. Serp, *Chem. – Eur. J.*, 2024, **30**, e202400669.
66 D. C. Gary, B. A. Glassy and B. M. Cossairt, *Chem. Mater.*, 2014, **26**, 1734–1744.
67 W.-S. Ojo, S. Xu, F. Delpech, C. Nayral and B. Chaudret, *Angew. Chem., Int. Ed.*, 2012, **51**, 738–741.
68 S. Fujii, S. Ishida and S. Asano, *J. Phys. F*, 1988, **18**, 971–980.
69 X. Xu, Y. Lu, J. Shi, X. Hao, Z. Ma, K. Yang, T. Zhang, C. Li, D. Zhang, X. Huang and Y. He, *Nat. Commun.*, 2023, **14**, 7708.
70 D. R. Aireddy and K. Ding, *ACS Catal.*, 2022, **12**, 4707–4723.

71 A. Ropp and S. Carenco, *Inorg. Chem.*, 2024, **63**, 17077–17086.
72 M. Li, X. Liu, Y. Xiong, X. Bo, Y. Zhang, C. Han and L. Guo, *J. Mater. Chem. A*, 2015, **3**, 4255–4265.
73 D. Yin, J. Tang, R. Bai, S. Yin, M. Jiang, Z. Kan, H. Li, F. Wang and C. Li, *Nanoscale Res. Lett.*, 2021, **16**, 11.
74 K. Kaźmierczak, D. Yi, A. Jaud, P.-F. Fazzini, M. Estrader, G. Viau, P. Decorse, J.-Y. Piquemal, C. Michel, M. Besson, K. Soulantica and N. Perret, *J. Phys. Chem. C*, 2021, **125**, 7711–7720.
75 C. Waldt, H. Montalvo-Castro, A. Almithn, Á. Loaiza-Orduz, C. Plaisance and D. Hibbitts, *J. Catal.*, 2023, **421**, 403–418.
76 M. M. Alsabban, M. K. Eswaran, K. Peramaiah, W. Wahyudi, X. Yang, V. Ramalingam, M. N. Hedhili, X. Miao, U. Schwingenschlögl, L.-J. Li, V. Tung and K.-W. Huang, *ACS Nano*, 2022, **16**, 3906–3916.
77 N. Jiang, B. You, M. Sheng and Y. Sun, *Angew. Chem.*, 2015, **127**, 6349–6352.
78 M. Shimizu, Y. Tsushima and S. Arai, *ACS Omega*, 2017, **2**, 4306–4315.
79 I. C. Gerber and P. Serp, *Chem. Rev.*, 2020, **120**, 1250–1349.
80 Q. Chen, I.-H. Svenum, L. Gavrilovic, D. Chen and E. A. Blekkan, *Surf. Sci.*, 2019, **681**, 24–31.
81 M. D. Navalikhina, N. E. Kavalerskaya, E. S. Lokteva, A. A. Peristyi, E. V. Golubina and V. V. Lunin, *Russ. J. Phys. Chem. A*, 2012, **86**, 1800–1807.
82 J. Navarro-Ruiz, C. Rivera-Cárcamo, B. Machado, P. Serp, I. Del Rosal and I. C. Gerber, *ACS Appl. Nano Mater.*, 2021, **4**, 12235–12249.
83 Y. Dai, X. Gao, X. Chu, C. Jiang, Y. Yao, Z. Guo, C. Zhou, C. Wang, H. Wang and Y. Yang, *J. Catal.*, 2018, **364**, 192–203.
84 J. Tan, J. Cui, T. Deng, X. Cui, G. Ding, Y. Zhu and Y. Li, *ChemCatChem*, 2015, **7**, 508–512.
85 H. Kim, S. Yang, Y. H. Lim, J. Lee, J.-M. Ha and D. H. Kim, *J. Catal.*, 2022, **410**, 93–102.
86 W. Chen, H. Xu, X. Ma, L. Qi and Z. Zhou, *Chem. Eng. J.*, 2023, **455**, 140565.
87 B. H. Arpini, J. L. Fiorio, J. V. F. da Costa, J.-O. Joswig and L. M. Rossi, *Catal. Sci. Technol.*, 2024, **14**, 1017–1025.
88 L. Zhao, X. Qin, X. Zhang, X. Cai, F. Huang, Z. Jia, J. Diao, D. Xiao, Z. Jiang, R. Lu, N. Wang, H. Liu and D. Ma, *Adv. Mater.*, 2022, **34**, 2110455.
89 J. Navarro-Ruiz, J. Audevard, M. Vidal, C. H. Campos, I. Del Rosal, P. Serp and I. C. Gerber, *ACS Catal.*, 2024, **14**, 7111–7126.
90 A. W. Augustyniak and A. M. Trzeciak, *Inorg. Chim. Acta*, 2022, **538**, 120977.
91 L. Xiang, H. Feng, M. Liu, X. Zhang, G. Fan and F. Li, *ACS Appl. Nano Mater.*, 2021, **4**, 4688–4698.
92 T. Kubota, H. Ogawa, Y. Okamoto, T. Misaki and T. Sugimura, *Appl. Catal., A*, 2012, **437–438**, 18–23.
93 C. Rivera-Cárcamo, C. Scarfiello, A. B. García, Y. Tison, H. Martinez, W. Baaziz, O. Ersen, C. Le Berre and P. Serp, *Adv. Mater. Interfaces*, 2021, **8**, 2001777.
94 F. Giraud, C. Geantet, N. Guilhaume, S. Loridant, S. Gros, L. Porcheron, M. Kanniche and D. Bianchi, *Catal. Today*, 2021, **373**, 69–79.
95 C. Scarfiello, K. Soulantica, S. Cayez, A. Durupt, G. Viau, N. Le Breton, A. K. Boudalis, F. Meunier, G. Clet, M. Barreau, D. Salusso, S. Zafeiratos, D. P. Minh and P. Serp, *J. Catal.*, 2023, **428**, 115202.
96 L. R. Merte, G. Peng, R. Bechstein, F. Rieboldt, C. A. Farberow, L. C. Grabow, W. Kudernatsch, S. Wendt, E. Lægsgaard, M. Mavrikakis and F. Besenbacher, *Science*, 2012, **336**, 889–893.
97 X. Zhao, J. Wang, L. Lian, G. Zhang, P. An, K. Zeng, H. He, T. Yuan, J. Huang, L. Wang and Y.-N. Liu, *ACS Catal.*, 2023, **13**, 2326–2334.
98 D. Gao, S. Wang, Y. Lv, C. Wang, J. Ren, P. Zheng, L. Song, A. Duan, X. Wang, G. Chen and C. Xu, *ACS Catal.*, 2024, **14**, 1939–1950.
99 J. Mazarío, S. Ghosh, V. Varela-Izquierdo, L. M. Martínez-Prieto and B. Chaudret, *ChemCatChem*, 2025, **17**, e202400683.